LAWRENCE
LIVERMORE
NATIONAL
LABORATORY

Evolution of a storm-driven cloudy boundary layer in the Arctic

J. Inoue, B. Kosovic, J. A. Curry

November 22, 2003

Disclaimer

This document was prepared as an account of work sponsored by an agency of the United States Government. Neither the United States Government nor the University of California nor any of their employees, makes any warranty, express or implied, or assumes any legal liability or responsibility for the accuracy, completeness, or usefulness of any information, apparatus, product, or process disclosed, or represents that its use would not infringe privately owned rights. Reference herein to any specific commercial product, process, or service by trade name, trademark, manufacturer, or otherwise, does not necessarily constitute or imply its endorsement, recommendation, or favoring by the United States Government or the University of California. The views and opinions of authors expressed herein do not necessarily state or reflect those of the United States Government or the University of California, and shall not be used for advertising or product endorsement purposes.

Evolution of a storm-driven cloudy boundary layer in the Arctic

Jun Inoue[1], Branko Kosović [2] and Judith A. Curry[1]

[1]School of Earth and Atmospheric Sciences
Georgia Institute of Technology, Atlanta, GA, U.S.A.

[2]Lawrence Livermore National Laboratory
Livermore, CA, U.S.A.

keywords: SHEBA, shear mixing, radiative cooling

short title: Storm-Driven Cloudy Boundary Layer

Corresponding author: Jun Inoue

School of Earth and Atmospheric Sciences
Georgia Institute of Technology
311 Ferst Dr.
Atlanta, Georgia 30332-0340 U.S.A.
Phone: 404-385-4414; FAX: 404-894-5638
e-mail: jun.inoue@eas.gatech.edu

24 October 2003

Abstract

The cloudy boundary layer under stormy conditions during the summertime Arctic has been studied using observation from the SHEBA experiment and large-eddy simulations (LES). On 29 July 1998, a stable Arctic cloudy boundary layer event was observed after passage of a synoptic low. The local dynamic and thermodynamic structure of the boundary layer was determined from aircraft measurement including analysis of turbulence, cloud microphysics and radiative properties. After the upper cloud layer advected over the existing cloud layer, the turbulent kinetic energy budget indicated that the cloud layer below 200 m was maintained predominantly by shear production. Observations of longwave radiation showed that cloud top cooling at the lower cloud top has been suppressed by radiative effects of the upper cloud layer. Our LES results demonstrate the importance of the combination of shear mixing near the surface and radiative cooling at the cloud top in the storm-driven cloudy boundary layer. Once the low-level cloud reaches a certain height, depending on the amount of cloud-top cooling, the two sources of TKE production begin to separate in space under continuous stormy conditions, suggesting one possible mechanism for the cloud layering. The sensitivity tests suggest that the storm-driven cloudy boundary layer is flexibly switched to the shear-driven system due to the advection of upper clouds or the buoyantly driven system due to the lack of the wind shear. A comparison is made of this storm-driven boundary layer with the buoyantly driven boundary layer previously described in the literature.

1 Introduction

Persistent stratus cloud layers over the Arctic Ocean are important modulators of the climate through the modulation of atmospheric radiation and vertical turbulent transfer of heat, moisture and momentum in the boundary layer. Understanding the effect of clouds on the surface is an especially vital issue because it can significantly impact the melting, refreezing, thickness and distribution of the sea ice (e.g., Maykut and Untersteiner, 1971). There are many physical processes related to clouds over the Arctic region which are still poorly understood (Curry et al., 1996; Bromwich et al., 1994).

The summertime Arctic stratus clouds are believed to be typically formed by the relatively warm and moist continental air as it flows over the pack ice which induces the condensation due to the radiative and diffusive cooling to the colder surface and longwave emission to space (Herman and Goody, 1976). Once the surface fog/cloud forms, vertical mixing induced by the cloud-top radiative cooling occurs. Analyzing a series of 12 vertical profiles in a variety of boundary layer stratus clouds in the summertime Arctic, Herman and Curry (1984) found that the observed low-level stratus cloud tops were typically 1000 m high and buoyancy driven. Some common features were also found in the North Sea stratocumulus (Nicholls, 1984). The radiatively driven cloud-topped boundary layers are often found to be decoupled (Nicholls and Leighton, 1986).

In addition to the low-level clouds, the mid- and upper-level clouds associated with synoptic frontal systems are sometimes advected over the existing lower clouds in the summertime Arctic. From the statistical study based on a radar and lidar at SHEBA (Intrieri et al., 2002), one of the highest cloud-top frequency is 6 to 8 km. These upper clouds may cause the decay of the lower clouds through suppression of cloud top radiative cooling. To understand the complicated structure

of cloud layering which has been observed frequently in the summertime Arctic (Intrieri et al., 2002), modeling studies focusing on the radiative transfer in the boundary layer have been conducted for the summertime Arctic boundary layer and formation of multiple cloud layers (McInnes and Curry, 1995; Herman and Goody, 1976). Although cyclonic events drive the seasonal transition through the changes in numerous surface energy budget terms, the surface temperature, and number and spatial coverage of open leads (Ruffieux et al., 1995; Persson et al., 2002; Curry et al., 2002), the combination of turbulent and radiative properties in the stormy cloudy boundary layer are still poorly understood.

To investigate the impact of turbulence on the boundary layer more explicitly, large-eddy simulation (LES) is a useful tool. The concept of the LES is to explicitly simulate the large eddies, which contain most of the energy and dominate turbulent fluxes within the boundary layer, and parameterize the subgrid-scale motions. In recent years, stably stratified boundary layers have been studied with an LES model (Mason and Derbyshire 1990; Andren, 1995; Kosović and Curry, 2000; Saiki et al., 2000; Otte and Wyngaard, 2001).

The goal of this study is to propose mechanisms for the evolution of the cloudy boundary layer under stormy conditions in the summertime Arctic. For this purpose, we use the aircraft observations from Surface Heat Budget of the Arctic Ocean (SHEBA), which was a year-long field program that employed a drifting ship station on the pack ice of the Arctic Ocean, in combination with remote sensing, aircraft observations and modeling analyses of the entire Arctic Basin (Perovich et al., 1999; Curry et al., 2000; Uttal et al., 2002). We focus on the observations of 29 July 1998 when a stable boundary layer with a surface cloud was observed, and simulate the boundary layer structure with an LES model (Kosović and Curry, 2000). Section 2 presents a description of the observations. The turbulent characteristics and radiative properties obtained by the observation are shown in sections

3 and 4, respectively. The physical processes of the stormy boundary layer are investigated using LES in section 5. Finally, we present a summary and conclusions in section 6.

2 Observations

2.1 Aircraft data

The National Center for Atmospheric Research (NCAR) C-130 Research Aircraft at the SHEBA ship at 78.50°N, 163.20°W flew on 29 July 1998 after passage of a synoptic low over the Arctic Ocean. The main objective of this flight was to obtain meteorological data within a cloudy boundary layer under stormy conditions. The capabilities of the NCAR C-130 and instrumentation on the aircraft are described in detail by Curry et al. (2000).

Measurements of atmospheric temperature, dew point, humidity, winds, turbulence, radiative fluxes, and microphysical data were obtained with the aircraft. Fast response (25 Hz) temperature, water vapor, and velocity data were collected with the Rosemount thermometer, Lyman-alpha hygrometer, and gust probes, respectively. Upward and downward shortwave and longwave broadband radiative fluxes were obtained with Eppley pyranometers and pyrgeometers. The King probe measured cloud liquid water contents.

The location of the flight is depicted in Figure 1. The flight patterns consisted of six level flights at least 30 km long below the 600 m level between 22:13 and 23:04 on 29 July, and two vertical soundings before and after those level flights. The length of each leg provides adequate horizontal statics for determination of variances and covariances.

2.2 Synoptic situation

To grasp the synoptic situation, Advanced Very High Resolution Radiometer (AVHRR) satellite imagery and NCEP reanalysis were used in this study. Ancillary data sets are cloud radar images obtained at SHEBA ship which was specifically designed by NOAA Environmental Technology Laboratory (ETL) for long-term continuous operation under Arctic conditions with an emphasis on the detection of Arctic clouds (Shupe et al., 2001; Intrieri et al., 2002). The meteorological tower data from the Atmospheric Surface Flux Group (ASFG) site and the sounding data from the GPS/Loran Atmospheric Sounding System (GLASS) are also used in this study.

In July and August 1998, the SHEBA camp was located on the pack ice in the Chukchi Sea near 78°N, 161-166°W. During these two months, several cyclonic events occurred, producing significant reduction in surface pressure (Figure 2-a). Especially from 26 July to 31 July, surface pressure and air temperature dropped 35 hPa and 2 K, respectively (Figures 2-a and -b). During this period, the precipitation began as rain but changed to ice pellets. At 23 UTC on 28 July, graupel or small hail (2.5 cm in diameter) were reported from the ship. And then finally precipitation changed to snow near 12 UTC on 29 July. As the result of the substantial ice divergence caused by the strong winds, the lead fraction increased from 5 to 14 % (Curry et al., 2002). Although Persson et al. (2002) reported that the onset of freezing started on 16 August 1998, passage of the cyclone at the end of July caused the increase of the albedo (Figure 2-c) through the glazing of the surface melt ponds associated with a drop of the surface air temperature and the accumulation of some snow on the ice (Curry et al., 2002).

On 29 July 1998, the low-level clouds behind the frontal system are evident in the infrared AVHRR satellite imagery (Figure 1), associated with the cold advection behind the frontal system (Figure

6

2-d). Figure 3 is the time-height cross section of the cloud radar reflectivity at the SHEBA site and coordinates of the boundary layer flight pattern. The boundary layer developed before the aircraft observation and decayed when the upper clouds were advected in.

2.3 Mean profiles

The vertical profiles of potential temperature, wind components, water vapor mixing ratio and liquid water contents (LWC) during vertical descent and ascent of the aircraft are plotted in Figure 4 along with the leg average profiles. The scatter among the instantaneous profiles is indicative of horizontal and temporal variability.

The boundary layer is characterized by two inversion layers associated with upper clouds at 2100 m level and lower clouds below 500 m level at 22 UTC. The wind is westerly, categorized as a cold advection regime behind a synoptic low (Figure 2-d). It is noted that u wind component has a strong shear near the surface below 200 m level. The v wind component has weaker wind shear up to 500 m level. Water vapor increases with height through the lower cloud layer reaching a peak value near 500 m.

According to the profiles of potential temperature and water vapor mixing ratio after one hour (thin lines in Figure 4), the top of the lower boundary layer decreased about 50 m. The maximum water vapor mixing ratio also decreased from 4.7 to 4.2 g kg^{-1}. This tendency can be also seen in LWC, in particular, the upper half of the layer decayed significantly from 0.3 to 0.2 g m^{-3}. However, the characteristics of wind components persist during the observation.

3 Turbulent structure

In this section, the turbulent properties of the cloudy boundary layer are examined using profiles of variances, turbulent heat and momentum flux, and turbulent kinetic energy (TKE).

3.1 Variance and flux profiles

Spectra and cospectra are calculated from the high-frequency temperature and velocity data collected during each leg, following Pinto (1998). The time series of each variable is partitioned into 60-s segments. By integrating over the spectrum and cospectrum, variance and covariance are calculated at each level. This time interval is chosen to produce the maximum number of data points possible while still adequately resolving the range of eddy sizes expected in the boundary layer. The 60-s segments for each variable are detrended and then separated into their mean and fluctuating components. These calculations are performed using data that have been filtered to omit the high-frequency noise generated by the aircraft.

Variance of vertical velocity ($\overline{w'^2}$), streamwise velocity ($\overline{u'^2}$), across-stream velocity ($\overline{v'^2}$), and potential temperature ($\overline{\theta'^2}$) are plotted in Figure 5-a. The $\overline{w'^2}$ shows a maximum at the lowest level and decreases almost linearly with height to cloud top. Streamwise and across-stream variances are much larger below 200 m due to the strong wind shear near the surface (Figure 4). The largest value of $\overline{\theta'^2}$ occurred at cloud top, which is attributed to entrainment and variations in cloud-top height (Lawson et al., 2001). Although $\overline{w'^2}$ and the turbulence production by buoyancy are not directly related, buoyant production may be small due to the small value of $\overline{w'^2}$ at this level.

Vertical profiles of heat and momentum flux are given in Figure 5-b. The negative heat flux near the surface indicates that the heat is transported toward the ice surface by the turbulent eddies.

The weak positive slope in the middle layer from 100 to 300 m indicates that the boundary layer is cooled by turbulent diffusion. The negative or near zero heat flux at the cloud top suggests the lack of sinking air from cloud top by the radiative cooling. The momentum flux of $\overline{u'w'}$ is largest near the surface and decreases towards the cloud top. This characteristic is not evident in $\overline{v'w'}$ where weak mean wind and wind shear are seen (Figure 4).

3.2 Turbulent kinetic energy budget

The buoyancy and shear production terms in the TKE budget are calculated to provide insight into the turbulent processes that determine the boundary layer structure. The turbulent transport, viscous dissipation, and pressure correlation terms are not calculated explicitly but may be inferred from the imbalance term assuming the TKE is in steady state following

$$I = -\overline{u'w'}\frac{\partial U}{\partial z} - \overline{v'w'}\frac{\partial V}{\partial z} + \frac{g}{T_0}\overline{w'\theta'_v} \tag{1}$$

where I is the imbalance term, the first two terms on the right represent shear production, and the third term on the right buoyancy production. The constant of gravity is denoted by g. The reference temperature T_0 is chosen to be the ice surface temperature. For the buoyancy production term, fluctuations in virtual potential temperature are approximated using potential temperature.

Using mean wind, turbulent stress, and heat flux profiles, the production of TKE from buoyancy and shear are obtained (Figure 5-c). After the upper cloud layer was advected over the existing cloud layer (Figure 3), the TKE budget indicates that the cloud layer below 200 m is maintained predominantly by shear production. The small value of the buoyancy term above this level indicates that the cloud top cooling may have been suppressed by radiative effects of the upper cloud layer. However, the gain of TKE is not necessarily zero in this layer because the turbulent transport is

included in the imbalance term (I). If the TKE produced by the radiatively cooled air at the advected upper cloud layer is transported downward into the lower layer, the structure of boundary layers is coupled.

4   Radiative properties of cloudy boundary layer

Radiative cooling in the cloudy boundary layer is important for development of a cloud-topped mixed layer. In multiple cloud layers, the vertical distributions of upward and downward longwave radiative fluxes become more complicated. Figure 6-a shows the profiles of upward and downward longwave radiative fluxes and LWC obtained by the aircraft descent at 22 UTC on 29 July. Two significant changes in the fluxes occurred at the cloud tops at 400 m and 2100 m. The downward longwave radiation at 2100 m sharply increases downward approximately 60 W m^{-2}, on the other hand, the increase of the flux at 400 m level is about 10 W m^{-2} in spite of larger amount of LWC than that of upper cloud layer. The difference between upward and downward radiation fluxes below 800 m level is almost constant (10 W m^{-2}), suggesting that the net flux divergence (i.e., heating rate) is very small. At the top of the upper cloud, on the other hand, a large difference between the fluxes is apparent, which causes a strong cooling over the layer.

To estimate the profile of the heating rate, a two-stream, narrow-band, radiative transfer model (Key, 2001) is employed. The observed surface temperature and profiles of temperature and moisture on 22 UTC 29 July 1998 were used as input for the model (see Figure 4 for thermodynamic structure). For the microphysics, the cloud thickness and LWC were determined by the profile of LWC. Cloud particle size at upper and lower clouds were set to 15 and 30 μm (as mentioned by Lawson et al., 2001), respectively.

Figure 6-b shows the profile of longwave heating rate estimated by the model (dashed line). The heating rate based on the observation calculated by the divergence of the net longwave radiation fluxes with 15 m resolution is also shown (thick line). The model provides a good estimate of the longwave radiative cooling rate. At the upper cloud top, the radiative cooling rate exceeds 45 K day^{-1} where strong mixing by cooled air should occur. The cooling rate of the lower cloud layer (more than 10 K day^{-1}), on the other hand, is smaller than that of upper cloud layer, resulting in the small buoyancy production of TKE. Therefore, the reason for the small contribution of buoyancy production of TKE at the lower cloud top (above 400 m level in Figure 5-c) comes from the radiative effect of the upper cloud layer.

Considering the decrease of boundary-layer height (Figure 4), the state of the upper half of this layer can be interpreted as a decaying stage, which makes the transport of cooled air mass and the resultant condensation small in the upper half of the layer. However, the transport process of TKE has not been understood yet due to the lack of aircraft observation at the upper cloud and cloud-free layers. Therefore, in next section, by using a large-eddy simulation, we investigate the coupled/decoupled structure of the stormy boundary layer and the role of buoyancy and shear production in the development and maintenance of the layer.

5 Large-eddy simulation

5.1 Model description

The basic dynamic framework of the LES model including the complete set of equations has been described in Kosović and Curry (2000). The parameterization of subgrid-scale (SGS) motion is based on Kosović's (1997) nonlinear model which is capable of reproducing the effects of backscatter of TKE

and of the SGS anisotropies characteristic for shear-driven flows. The upper boundary condition is a radiative boundary condition, permitting internal gravity waves to propagate through the upper boundary (Klemp and Duran, 1983). Numerical algorithm is pseudospectral in horizontal planes and thus lateral boundary conditions are periodic. The resolution for each direction is 25 m (60^3 grid points). Time step for the simulation is 3.6 seconds.

To take into account for the cloud condensation process, a bulk parameterization scheme is adopted. This scheme assumes immediate conversion of any supersaturated vapor to liquid water. If the total moisture mixing ratio in a grid box is greater than the saturation vapor mixing ratio, the model assumes that clouds fill that grid box; otherwise, it assumes the grid box to be cloud-free.

For the radiation process used in this study, the radiative transfer is limited only to longwave radiative flux which is determined by using the mixed emissivity concept (Herman and Goody, 1976). This subroutine is used every 4 time steps.

The initial conditions, surface heat fluxes, and strength of inversion for simulations were based on the measurements made during SHEBA on 29 July 1998. The potential temperature profile was initialized so that it could develop into the observed profile after several hours of simulation. The initial surface temperature was set at 273 K. An inversion was specified above 450 m in all the simulations. Because of the lack of wind data of the radio sondes, the initial wind profile is constructed by the ECMWF reanalysis data and tower data at the SHEBA site.

The simulations were initiated at 06:00 UTC on 29 July 1998 and integrated for 24 hours. In the control simulation (CTR), the latitude was 78.5°N, the geostrophic westerly wind was set to 8 m s^{-1}, the surface cooling rate was 0.25 K h^{-1}, and surface roughness was 0.1 m. In additional simulations, we varied the basic parameters: without wind shear (NOSHEAR); and without radiative process

12

after 12 hours in the CTR (NORAD).

5.2 LES results

Figure 7-a shows the time-height cross sections of potential temperature and liquid water content for the CTR case. The boundary layer developed over a depth from 500 to 1200 m during 24 hours. The potential temperature in the layer gradually decreased from 273 to 271 K due to the cooling from surface and cloud top. The layer is always filled with clouds at each level. During the last three hours, the stratification near the surface became more stable with increase of liquid water content.

Figure 8 shows the time-height cross section of each TKE budget term for the CTR case (S, shear production; B, buoyancy production; T, transport; and D, dissipation). The TKE structure can be divided into two stages. One is a developing stage with cloud-filled boundary layer. Near the surface, the balance of TKE results from a balance between shear production (gain) and dissipation (loss) with smaller contributions from buoyancy (loss). Below the cloud top, on the other hand, buoyancy (gain) which comes from the radiative cooling balances with dissipation (loss). The TKE produced near the surface and cloud top is transported into the middle layer. The TKE budget during the developing stage can be summarized as follows: the shear-driven boundary layer and cloud-topped elevated mixed layer are coupled by transporting TKE into the middle layer.

The other stage is a mature stage which has decaying production by shear near the surface and buoyancy production at the cloud top. Unlike the developing stage, there is no net transport of TKE into the middle layer, suggesting the structure of boundary layer is essentially decoupled between the shear-driven layer and cloud-topped mixed layer. The boundary-layer development has been almost finished since the TKE structure decoupled.

5.3 Mechanism of cloud layering

For the formation of multiple cloud layers, two sources of TKE production are fundamentally important. One is the strong shear production over ice surface which potentially induces a single cloud layer through the shear mixing under the negative buoyant production near the surface. This works as the onset of formation of low-level cloud after a cyclonic event. Figure 9-a shows the comparison of TKE budget profiles between the CTR case after 24 hours and the observational results. Although the situations between the CTR and observation are different in terms of the number of cloud layer and the height of boundary layer, the modeled TKE structure is similar to that of observation below 500 m level. This means that the lower part of boundary layer is potentially maintained under conditions of strong wind shear.

The second source of TKE production is radiative cooling at the cloud top, which modulates the evolution of the boundary layer after the formation of a low level cloud. In the NOSHEAR case, the boundary-layer clouds with cloud-free layer developed higher than that in the CTR (Figure 7-b). In the NORAD case, on the other hand, the development of boundary layer stopped after radiative process was turned off (Figure 7-c). These results mean that the radiative cooling at the cloud top is important only for the development of the boundary layer. However, as the boundary layer develops, the cooled air can not be transported towards the lower level to which the shear mixing reaches, suggesting the amount condensation will decrease. Figure 10 shows the vertical distributions of tendencies of liquid cloud and static stability for the CTR case after 24 hours. The amount of cloud increases in the stable layer below 300 m and decreases in the neutral layer, which will divide the layer into cloud and cloud-free layers. The cloud-free layer in the NOSHEAR case (Figure 7-b) can be considered to be a special case when the cloud-free layer appears by the decoupling of TKE

without the low-level cloud. Therefore, the decoupling of TKE is the beginning of cloud layering.

From the viewpoint of the observational results, the NORAD case can be regarded as the case which the upper cloud layer advected over the existing lower cloud layer. The TKE profile of NORAD is also similar to that of observation (Figure 9-b). Although the boundary layer is filled with cloud below 800 m level, the production of TKE is limited below 200 m level which causes a more strongly stratified surface layer with increase of liquid cloud (Figure 7-c). Considering the TKE structures between the CTR and NORAD, the boundary layer clouds tend to be separated in space whether there is strong cloud topped cooling or not (i.e., whether or not there is an upper level cloud). This may be one of the reasons that cloud layering frequently occurs during the Arctic summer.

6   Concluding Remarks

Arctic stratus clouds under stormy conditions were investigated using aircraft observations and LES model for the case of 29 July 1998 during the SHEBA field program. After passing frontal system, a shallow cloud layer over the ice surface was formed and developed from 500 to 1000 m. The aircraft observations were carried out when the upper level cloud associated with a subsequent synoptic frontal system advected over the existing cloud layer, and showed that the TKE structure of lower cloud layer was maintained by a strong shear production within the lower part of the layer (below 200 m). In the upper part of the layer from 200 to 500 m, the production of TKE by shear and buoyancy was insignificant. The profiles of longwave radiation and heating rate based on the observations showed that the existence of the upper cloud which emitted downward longwave radiation suppresses the radiative cooling and resultant turbulent mixing in the lower cloud.

Three LES experiments were conducted to study the physical processes of the stormy cloudy

boundary layer in detail. The simulated boundary layer developed differently among these runs; in the control case, the cloud-filled boundary layer developed from 500 to 1200 m; in the case without wind shear, the cloud-topped boundary layer with cloud-free layer developed higher than the control case; and in the simulation without radiative process after 12 hours of the control case, the development of cloud-filled boundary layer was suppressed. Comparing the TKE structures among three runs, the shear production near the surface under negative buoyant flux potentially has the effect of maintaining the low-level cloud and making the layer more stable. The mixing by radiatively cooled air at the cloud top develops the layer vertically.

Once the cloud forms by shear mixing associated with cooling near the ice surface, the cloud-topped mixed layer gradually develops by radiative cooling (e.g., the control case). The production of TKE in the developing stage is coupled between the shear mixed layer and cloud-topped mixed layer through the TKE transport into the middle layer. However, once the cloud reaches a certain height depending on the amount of cloud-top cooling, the two sources of TKE production begin to separate in space because the TKE can not be sufficiently transported into the middle layer. Smaller transport of the cooled air into the middle layer causes less condensation, making a cloud-free layer which divide between lower and upper cloud layers. This self-separation of the TKE structure is one possible mechanism for cloud layering under stormy conditions.

Another feature of the storm-driven cloudy boundary layer is that the low level cloud persists under the strong wind shear condition near the surface even if the upper layer cloud associated with a cyclone is advected over the layer. The TKE structure of our simulation without radiative cooling had the same characteristics as the observations with a strong shear production in lower half of the cloud layer and a weak buoyancy in upper half of the layer. This means that the existence of the

16

lower cloud layer is prevented from further development and is maintained at only where the shear mixing reaches. This is one of the reasons that June and July are the only two months in which the fraction of time with multiple layers greatly exceeds the fraction of time with single cloud layers (e.g., Intrieri et al., 2002).

In this study, the effects of large-scale vertical motions and precipitation are not included in our LES model. Investigating the effects of radiation, large-scale vertical motion and drizzle, McInnes and Curry (1995) showed that radiative cooling under the weak rising vertical motion was the most favorable situation for the maintenance of the multiple cloud layers. The effect of drizzle on the cloud layering was small unless the rising vertical motion was absent. The remarkable contrast between McInnes' buoyantly driven and our storm-driven boundary layers is the existence of thick shear-mixing layer (200~300 m) which is comparable with that of buoyantly mixed layer near the cloud top (Figure 8). Under stormy conditions, the coupling between the shear-driven and buoyantly driven layers is strong enough to maintain the low-level cloud without the large-scale vertical motions. In addition, once the wind shear weakens, the boundary layer will shift to the buoyantly driven system with cloud-free layer (Figure 7-b), while once another upper cloud advects, the boundary layer shifts to a shear-driven system (Figure 7-c). In the observation, in fact, the lower cloud persisted for more than three hours as a shear-driven boundary layer (Figure 3). Therefore, the storm-driven cloudy boundary layer as a whole can be regarded as a long-lived system.

Acknowledgments.

References

Andren, A.: 1995, 'The Structure of Stable Stratified Atmospheric Boundary Layers: A Large-Eddy Simulation Study', *Quart. J. Roy. Meteor. Soc.*, **121**, 961-985.

Bromwich, D. H., Tzeng, R.-Y., and Parish, T. R.: 1994, 'Simulation of the Modern Arctic Climate by the NCAR CCM1', *J. Climate.*, **7**, 1050-1069. 715-746.

Curry, J. A., Rossow, W. B., Randall D., and Schramm, J. L.: 1996, 'Overview of Arctic Cloud and Radiation Characteristics', *J. Climate*, **9**, 1731-1764.

Curry, J. A., and 26 Coauthors: 2000, 'FIRE Arctic Clouds Experiment', *Bull. Amer. Meteor. Soc.*, **81**, 5-29.

Curry, J. A., Schramm, J. L., Alam, A., Reeder, R., Arbetter, T. E., and Guest, P.: 2002, 'Evaluation of Data Sets Used to Force Sea Ice Models in the Arctic Ocean', *J. Geophys. Res.*, **107**, doi:10.1029/2000JC000466.

Herman, G. F., and Goody, R.: 1976, 'Formation and Persistence of Summertime Arctic Stratus Clouds', *J. Atmos. Sci.*, **54**, 2799-2812.

Herman, G. F., and Curry, J. A.: 1984, 'Observational and Theoretical Studies of Solar Radiation in Arctic Stratus Clouds', *J. Climate Appl. Meteor.*, **23**, 5-24.

Intrieri, J. M., Shupe, M. D., Uttal, T., and McCarty, B. J.: 2002, 'An Annual Cycle of Arctic Cloud Characteristics Observed by Radar and Lidar at SHEBA', *J. Geophys. Res.*, **107**, 8030, doi:10.1029/2000JC000432.

Key, J.: 2001, 'Streamer User's Guide', *Cooperative Institute for Meteorological Satellite Studies*, University of Wisconsin, 96 pp.

Klemp, J. B., and Duran, D. R.: 1983, 'An Upper Boundary Condition Permitting Internal Gravity Wave Radiation in Numerical Meso-Scale Models', *Mon. Wea. Rev.*, **111**, 430-444.

Kosović, B.: 1997, 'Subgrid-Scale Modeling for the Large-Eddy Simulation of High-Reynolds-Number Boundary Layers', *J. Fluid Mech.*, **336**, 151-182.

Kosović, B., and Curry, J. A.: 2000, 'A Large Eddy Simulation Study of a Quasi-Steady, Stably Stratified Atmospheric Boundary Layer', *J. Atmos. Sci.*, **57**, 1052-1068.

Lawson, R. P., Baker, B. A., Schmitt, C. G., and Jensen, T. L.: 2001, 'An Overview of Microphysical Properties of Arctic Clouds Observed in May and July 1998 during FIRE ACE', *J. Geophys. Res.*, **106**, 14989-15014.

Mason, P. J., and Derbyshire, S. H.: 1990, 'Large-Eddy Simulation of the Stably-Stratified Atmospheric Boundary Layer', *Boundary-Layer Meteorol.*, **42**, 117-162.

Maykut, G. A., and Untersteiner, N.: 1971, 'Some Results from a Time-Dependent Thermodynamic Model of Sea Ice', *J. Geophys. Res.*, **76**, 1550-1575.

McInnes, K., and Curry, J. A.: 1995, 'Modeling the Mean and Turbulent Structure of the Summertime Arctic Cloudy Boundary Layer', *Boundary-Layer Meteorol.*, **73**, 125-143.

Nicholls, S.: 1984, 'The Dynamics of Stratocumulus: Aircraft Observations and Comparisons with a Mixed Layer Model', *Quart. J. Roy. Meteor. Soc.*, **110**, 783-820.

Nicholls, S., and Leighton, J.: 1986, 'An Observational Study of the Structure of Stratiform Cloud Sheets: Part I. Structure', *Quart. J. Roy. Meteor. Soc.*, **112**, 431-460.

Otte, M. J., and Wyngaard, J. C.: 2001, 'Stably Stratified Interfacial-Layer Turbulence from Large Eddy Simulations', *J. Atmos. Sci.*, **58**, 3424-3442.

Perovich, D. K., and 22 Coauthors: 1999, 'Year on Ice Gives Climate Insights', *EOS, Trans. Amer. Geophys. Union*, **80**, 481-486.

Persson, P. O. G., Fairall, C. W., Andreas, E. L., Guest, P. S., and Perovich, D. K.: 2002, 'Measurements near the Atmospheric Surface Flux Group Tower at SHEBA: Near-Surface Conditions and Surface Energy Budget', *J. Geophys. Res.*, **107**, 8045, doi:10.1029/2000JC000705.

Pinto, J. O.: 1998, 'Autumnal Mixed-Phase Cloudy Boundary Layers in the Arctic', *J. Atmos. Sci.*, **55**, 2016-2038.

Ruffieux, D. R., Persson, P. O. G., Fairall, C. W., and Wolfe, D. E.: 1995, 'Ice Pack and Lead Surface Energy Budgets during LEADEX 92', *J. Geophys. Res.*, **100**, 4593-4612.

Saiki, E. M., Moeng, C.-H., and Sullivan, P. P.: 2000, 'Large-Eddy Simulation of the Stably Stratified Planetary Boundary Layer', *Boundary-Layer Meteorol.*, **95**, 1-30.

Shupe, M. D., Uttal, T., Matrosov, S. Y., and Frisch, A. S.: 2001, 'Cloud Water Contents and Hydrometeor Sizes during the FIRE Arctic Clouds Experiment', *J. Geophys. Res.*, **106**, 15015-15028.

Uttal, T., and 27 Coauthors: 2002, 'Surface Heat Budget of the Arctic Ocean', *Bull. Amer. Meteor. Soc.*, **83**, 255-275.
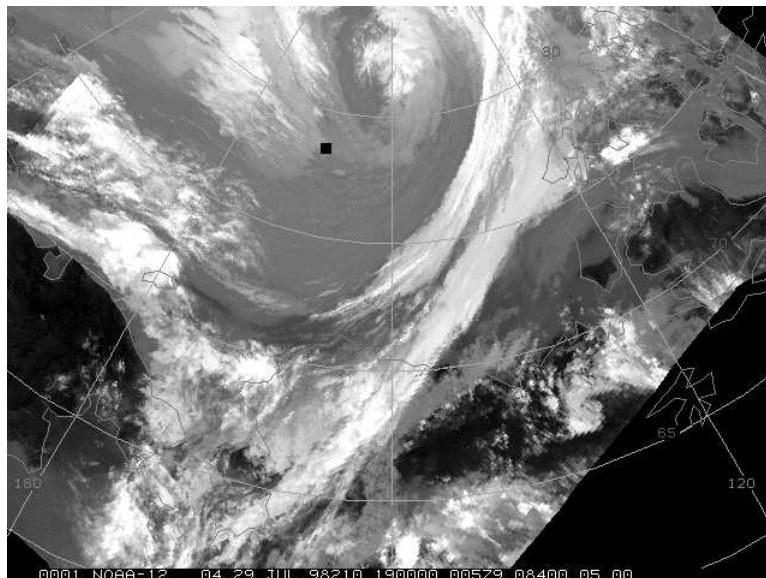
Figure Captions

Figure 1. AVHRR infrared satellite image on 19:00 UTC 29 July 1998. The location of SHEBA ship is depicted by a closed squre.
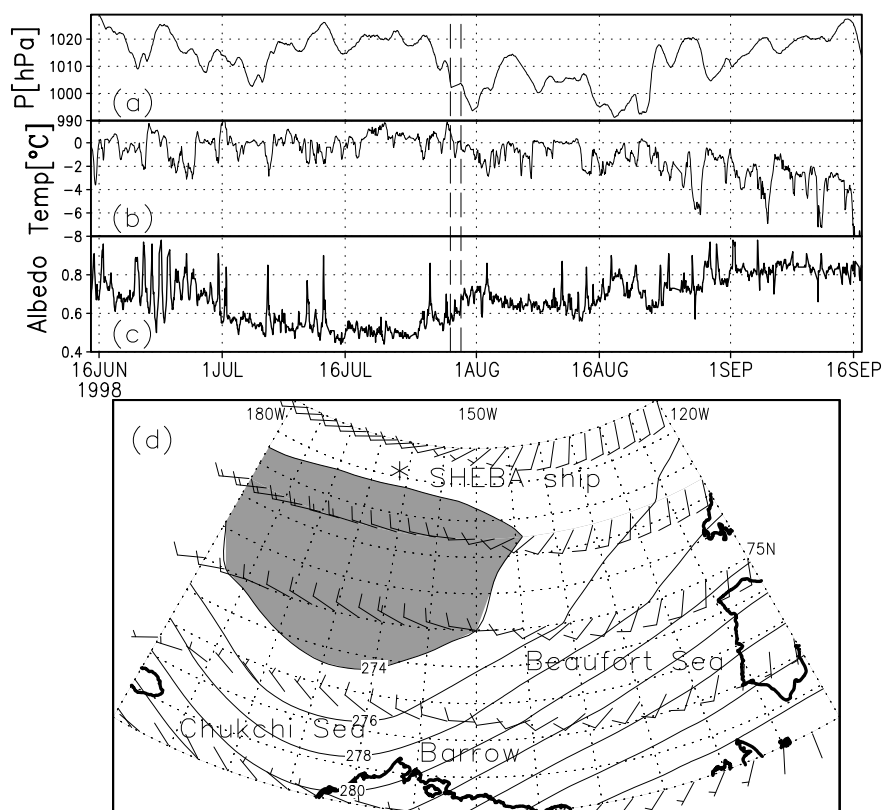
Figure 2. Time series of (a) surface pressure, (b) air temperature at 10 m level and (c) albedo obtained by the SHEBA tower, and (d) horizontal distribution of air temperature and wind fields at 1000 hPa by NCEP reanalysis for 18 UTC 29 July 1998. The asterisk denotes the location of the SHEBA ship and flight campaign. The gray area denotes cold area below 274 K. Dashed lines denote the period of 29 July 1998.

Figure 3. Time-height cross sections of radar reflectivity at SHEBA observation site and flight coordinate of C-130 on 29 July 1998.

Figure 4. Profiles of potential temperature (K), u and v wind (m s^{-1}), water vapor mixing ratio (g kg^{-1}) and liquid water contents (g m^{-3}) obtained from air craft descent and ascent for 22:00-22:15 (thick line) and 23:15-23:30 (thin line) on 29 July. The circles represent leg-average values.

Figure 5. Profiles of (a) average variance in vertical velocity $< w^2 >$, streamwise velocity $< u^2 >$, across-stream velocity $< v^2 >$, and potential temperature $< \theta^2 >$, (b) fluxes of heat $< w\theta >$, streamwise momentum $< uw >$, and across-stream momentum $< vw >$, and (c) turbulent kinetic energy budget terms determined from aircraft measurements (S: shear production (solid); B, buoyancy (dotted); and I, imbalance term (dashed)).

Figure 6. Profiles of (a) upward (thin line) and downward (thick line) longwave radiative flux obtained by the aircraft descent on 22 UTC 29 on July 1998, and (b) longwave heating rate

calculated by using 15 m resolution with the observation (thick line) and by the radiative

transfer model (dashed line). Liquid water contents are also depicted by the gray area.

Figure 7. Time height cross sections of potential temperature (solid line) and liquid water contents

(gray area) for each case.

Figure 8. Time height cross section of each TKE budget term in the CTR case (S: shear production;

B, buoyancy; T, transport; and D, dissipation).

Figure 9. TKE budget for (a) CTR and (b) NORAD cases after 24 hours. Thick line, TKE

production; thin line, buoyant term; dashed line, dissipation term. Observational results are

also depicted by + (production), * (buoyancy), and × (imbalance).

Figure 10. Vertical distributions of (a) time change of liquid cloud and (b) static stability for the

CTR after 24 hours simulation.

Fig. 1: AVHRR infrared satellite image on 19:00 UTC 29 July 1998. The locatoin of SHEBA ship is depicted by a closed squre.

Fig. 2: Time series of (a) surface pressure, (b) air temperature at 10 m level and (c) albedo obtained by the SHEBA tower, and (d) horizontal distribution of air temperature and wind fields at 1000 hPa by NCEP reanalysis for 18 UTC 29 July 1998. The asterisk denotes the location of the SHEBA ship and flight campaign. The gray area denotes cold area below 274 K. Dashed lines denote the period of 29 July 1998.

24
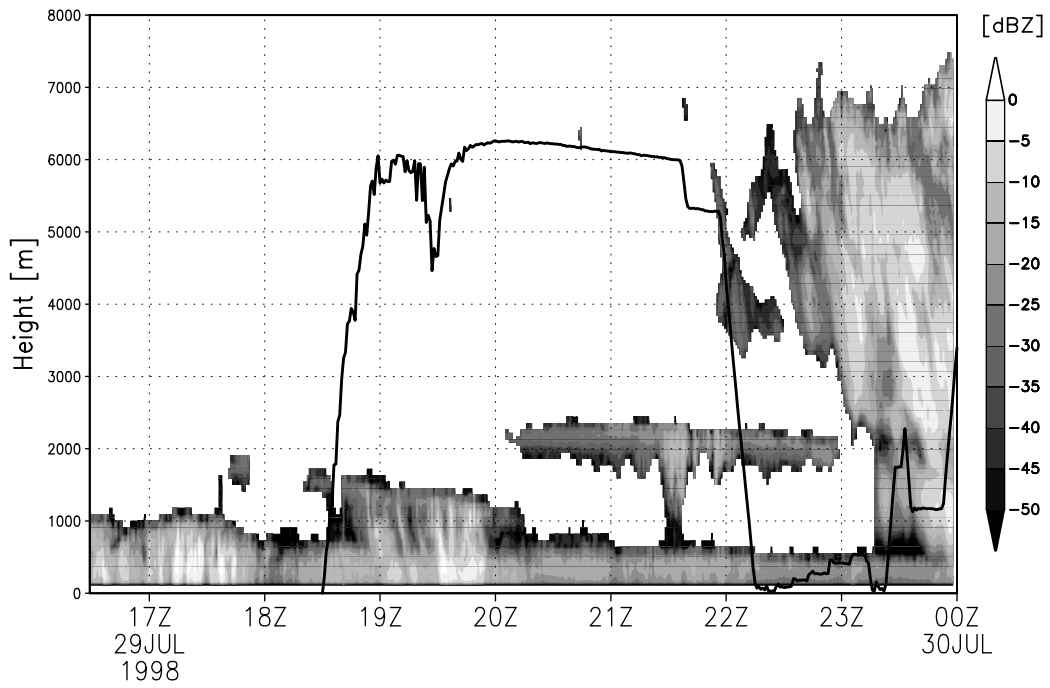
Fig. 3: Time-height cross sections of radar reflectivity at SHEBA observation site and flight coordinate of C-130 on 29 July 1998.
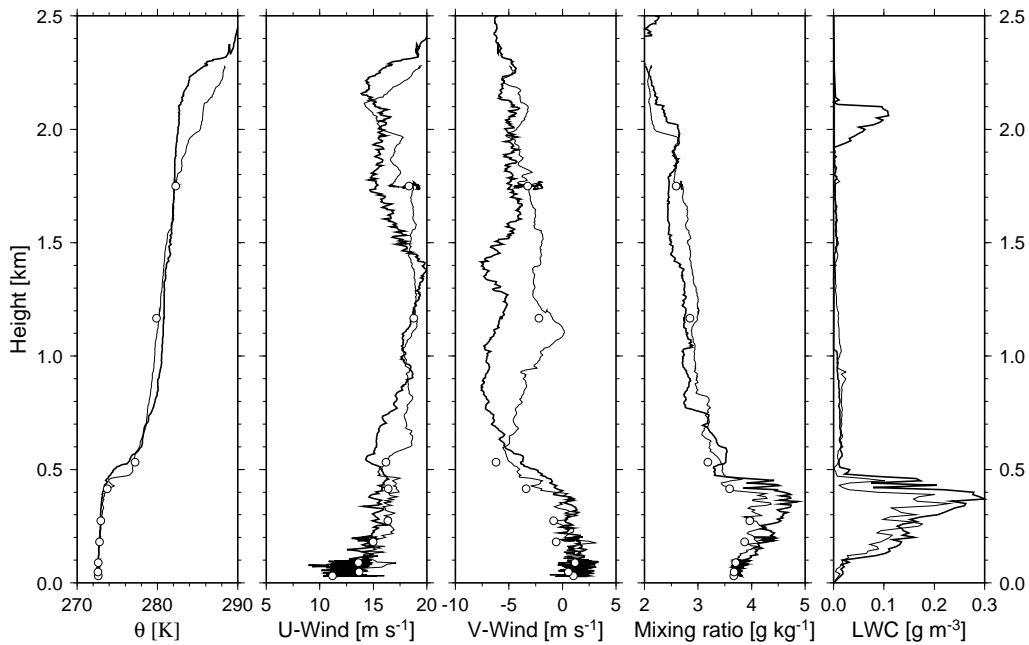
Fig. 4: Profiles of potential temperature (K), u and v wind (m s^{-1}), water vapor mixing ratio (g kg^{-1}) and liquid water contents (g m^{-3}) obtained from air craft descent and ascent for 22:00-22:15 (thick line) and 23:15-23:30 (thin line) on 29 July. The circles represent leg-average values.
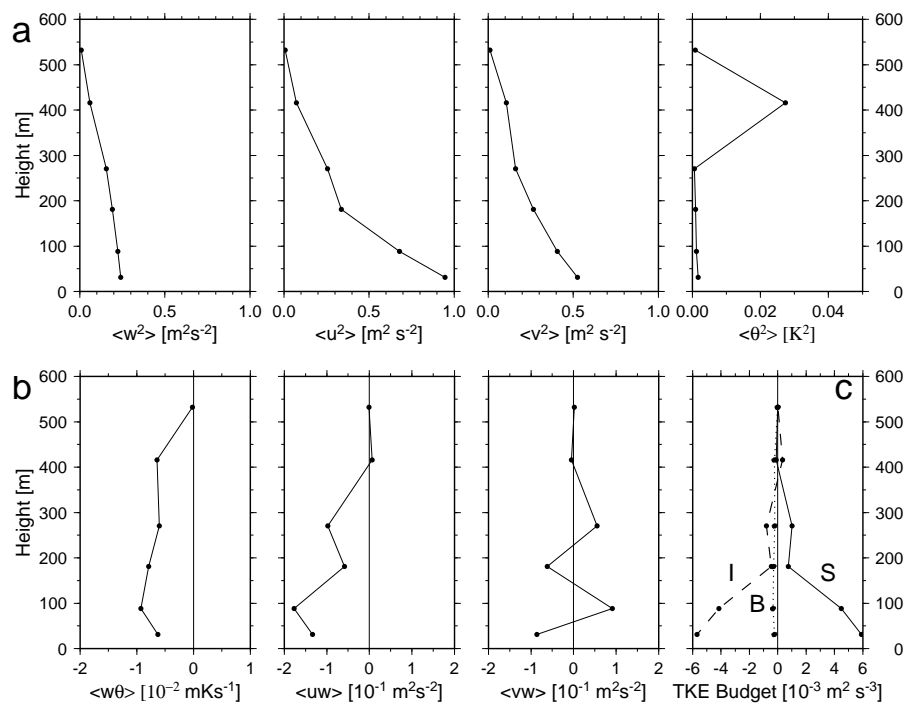
Fig. 5: Profiles of (a) average variance in vertical velocity $< w^2 >$, streamwise velocity $< u^2 >$, across-stream velocity $< v^2 >$, and potential temperature $< \theta^2 >$, (b) fluxes of heat $< w\theta >$, streamwise momentum $< uw >$, and across-stream momentum $< vw >$, and (c) turbulent kinetic energy budget terms determined from aircraft measurements (S: shear production (solid); B, buoyancy (dotted); and I, imbalance term (dashed)).
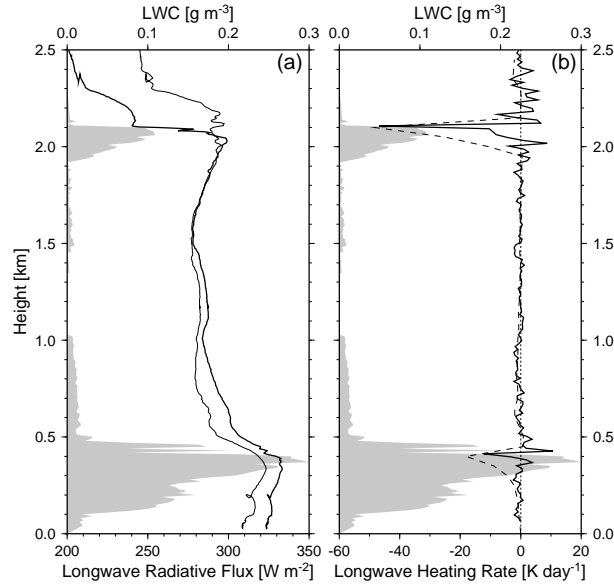

Fig. 6: Profiles of (a) upward (thin line) and downward (thick line) longwave radiative flux obtained by the aircraft descent on 22 UTC 29 on July 1998, and (b) longwave heating rate calculated by using 15 m resolution with the observation (thick line) and by the radiative transfer model (dashed line). Liquid water contents are also depicted by the gray area.
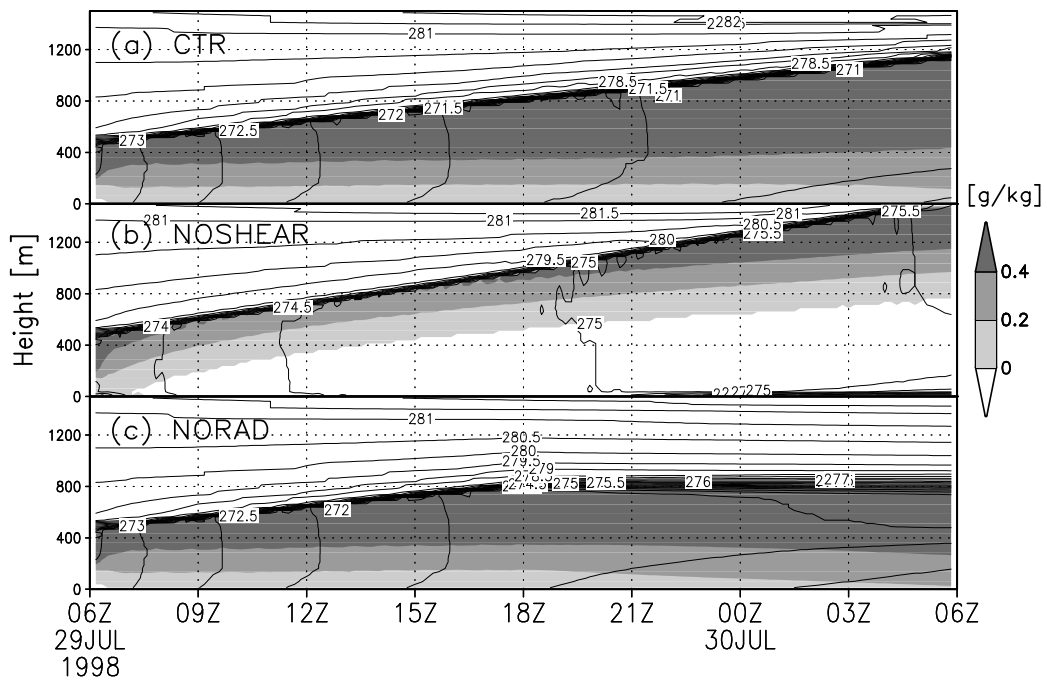
Fig. 7: Time height cross sections of potential temperature (solid line) and liquid water contents (gray area) for each case.
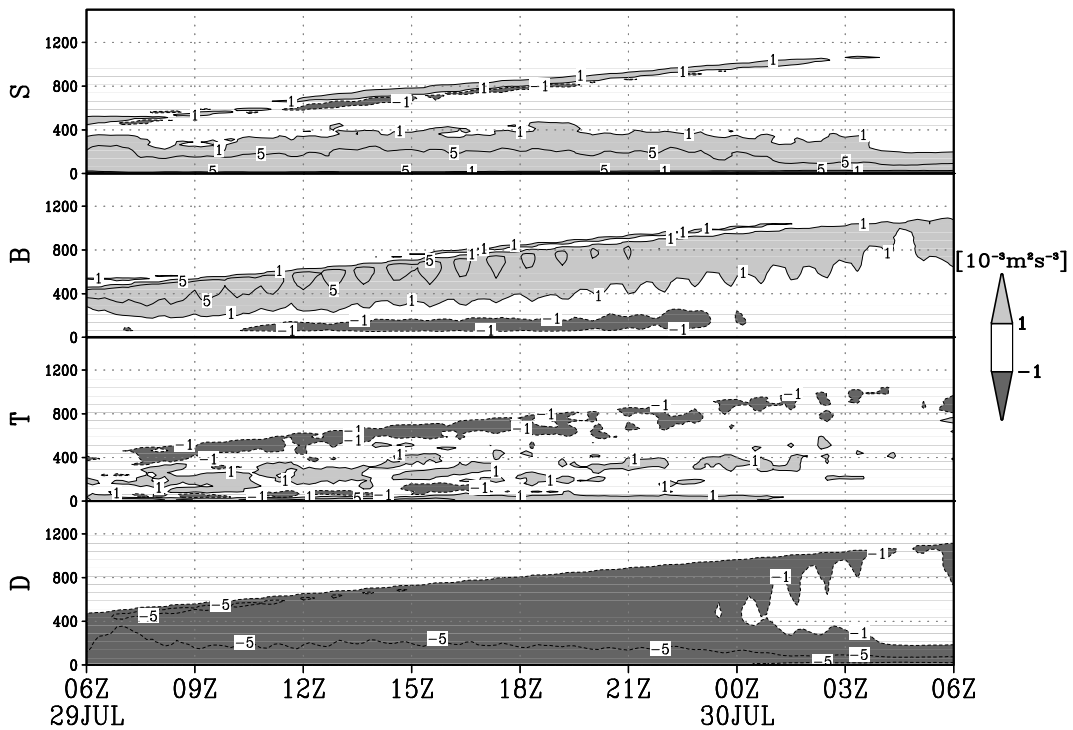

Fig. 8: Time height cross section of each TKE budget term in the CTR case (S: shear production; B, buoyancy; T, transport; and D, dissipation).
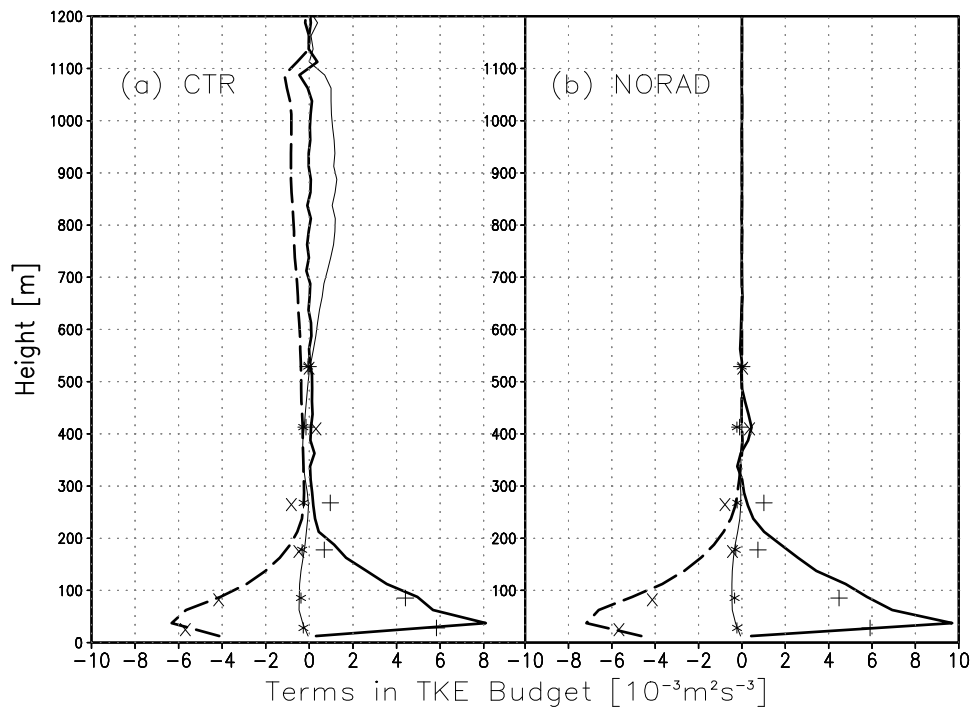
27

Fig. 9: TKE budget for (a) CTR and (b) NORAD cases after 24 hours. Thick line, TKE production; thin line, buoyant term; dashed line, dissipation term. Observational results are also depicted by + (production), ∗ (buoyancy), and × (imbalance).
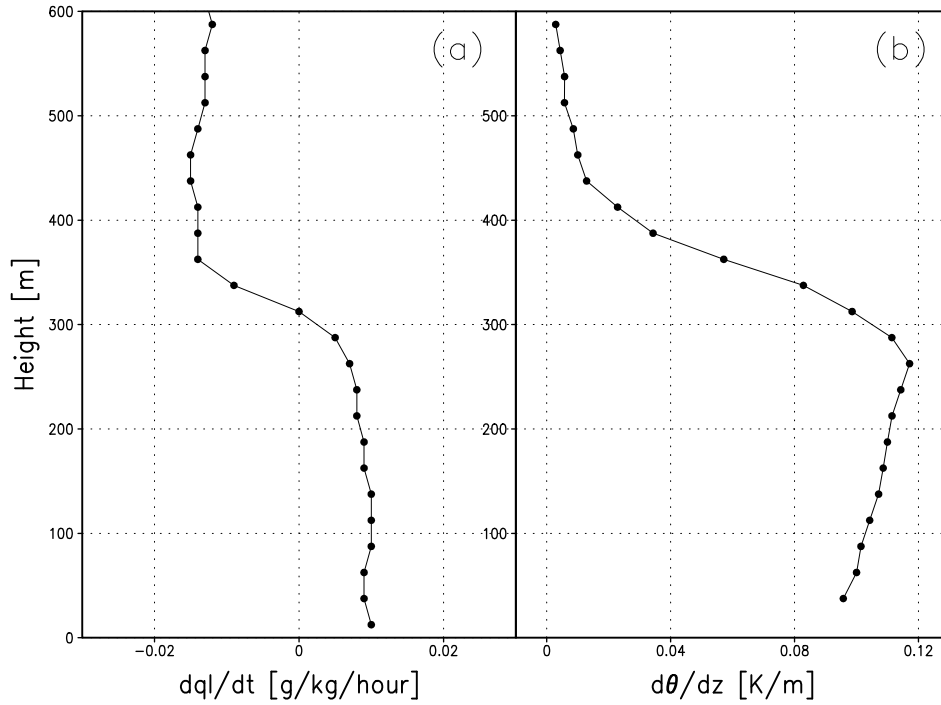

Fig. 10: Vertical distributions of (a) time change of liquid cloud and (b) static stability for the CTR after 24 hours simulation.